Available online at www.sciencedirect.com
ScienceDirect
Comput. Methods Appl. Mech. Engrg. 315 (2017) 760–779
Computer methods in applied mechanics and engineering
www.elsevier.com/locate/cma

Homogenization of the Navier-Stokes equations by means of the Multi-scale Virtual Power Principle

P.J. Blanco[a,d,*], A. Clausse[b,c], R.A. Feijóo[a,d]

[a] LNCC/MCTI Laboratório Nacional de Computação Científica, Av. Getúlio Vargas 333, Quitandinha, 25651-075, Petrópolis, Brazil
[b] CNEA-CONICET Comisión Nacional de Energía Atómica, Argentina
[c] UNC Universidad Nacional del Centro, 7000 Tandil, Argentina
[d] INCT-MACC Instituto Nacional de Ciência e Tecnologia em Medicina Assistida por Computação Científica, Petrópolis, Brazil

Received 29 September 2016; accepted 19 November 2016
Available online 25 November 2016

Highlights

- The Method of Multiscale Virtual Power is used to derive a novel two-scale model for fluid mechanics.
- The model targets the multiscale study of fluid flow in permeable media.
- Model capabilities are demonstrated in controlled study cases and in a comparison against DNS.
- The model is capable of retrieving complex fine-scale interactions observable at a coarse scale.

Abstract

This work addresses the multi-scale modeling of fluid flow in highly complex media based on the concept of Representative Volume Element (RVE). The Method of Multi-scale Virtual Power developed by the authors is employed to construct a coarse-scale model from standard fluid flow model at a fine-scale. Kinematic conservation principles, duality arguments and the balance of virtual power between scales are employed to set the grounds of the scale transition of physical fields. This allows to derive in a variationally consistent manner (i) the fine-scale problem to be solved at the RVE, and (ii) the homogenization formulae for coarse-scale dual quantities, namely, the force-like and stress-like fields. Examples of application of flow in permeable media are presented to show the potential of the present approach.

Keywords: Multi-scale; Fluid mechanics; Representative volume element; Virtual power; Permeable media

1. Introduction

Multi-scale simulation applied in the field of fluid mechanics has been largely acknowledged as a powerful tool to model complex flows, with special focus in the modeling of fluid flow through porous media. Furthermore, current

* Corresponding author at: LNCC/MCTI Laboratório Nacional de Computação Científica, Av. Getúlio Vargas 333, Quitandinha, 25651–075, Petrópolis, Brazil.
E-mail addresses: pjblanco@lncc.br (P.J. Blanco), clausse@exa.unicen.edu.ar (A. Clausse), feij@lncc.br (R.A. Feijóo).

http://dx.doi.org/10.1016/j.cma.2016.11.022
0045-7825/

technological developments aimed at manufacturing microstructures to attain complex, and often counterintuitive, media properties, pose new challenges to descriptive and predictive modeling [1–5].

The typical problem in which multi-scale modeling has been successfully applied is porous media flow, providing closure forms for Darcy-like constitutive equations [6–10]. However, there are still open questions about the generalization of these models to highly permeable media, that is, media in which the porosity is high. In this regard, multi-scale modeling can definitely help to elucidate the coarse-scale implications of fine-scale intricate phenomenology.

The asymptotic approach has been the preferred strategy to develop multi-scale models in fluid mechanics as proposed in Allaire's seminal work [11–13]. A myriad of applications concerning Stokes flow in porous media has benefited from this technique [14,7,8], and further extensions were proposed for the complete Navier-Stokes equations [15–19]. The common feature of all those applications is that small-scale physical phenomena are governed by viscous dissipation, and therefore the coarse-scale observable phenomena display a Darcy-like behavior. Another useful application of the multi-scale paradigm is the derivation of closure equations for turbulence models by means of asymptotic analysis [20]. The asymptotic strategy considers separation of scales as one of the milestones and assumes periodic conditions for fine-scale flows. It should be noted that there are a number of situations in which these two hypotheses do not hold and such models can yield misleading results.

Within the field of solid mechanics, multi-scale modeling has traditionally been supported by solid theoretical grounds originally established in the landmark works of R. Hill [21] and J. Mandel [22]. The so-called principle of macro-homogeneity (also known as Hill–Mandel principle) has been exhaustively explored in the characterization of complex material behavior, resulting in an approach that relies on the concept of Representative Volume Element (RVE). This is also widely known as computational homogenization approach [23–27]. In contrast, in the field of fluid mechanics, the RVE-based approach has been largely underused. To our knowledge, the only preliminary application of the Hill–Mandel principle in flow problems is the homogenization of a Stokes flow recently presented in [28]. However, the extension of this multi-scale modeling strategy to general flow conditions is still an open issue.

In turn, a unified theoretical framework for the formulation of RVE-based multi-scale models has been proposed in [29], based on the so-called Method of Multi-scale Virtual Power (MMVP). In a nutshell, MMVP relies on three pillars: (1) kinematic coupling between scales, (2) mathematical duality, and (3) the Principle of Multi-scale Virtual Power to physically couple the scales. Such approach has been employed to account for fine scale phenomena into coarse scale physics in several problems, such as the analysis of solids with micro-inertia [30], high order homogenization [31], thermoelasticity [32] and the analysis of material failure [33,34].

In the present article, the MMVP is exploited within the context of fluid mechanics to develop a coarse-scale flow model by properly homogenizing the steady-state Navier-Stokes equations at a fine-scale describing the flow of an incompressible fluid amid small obstacles. It is shown that the MMVP naturally leads to consistent homogenization formulae, retrieving force-like and stress-like coarse-scale closure equations from the homogenization of fine-scale phenomena in a parameter-free setting. The potential of the MMVP is shown by unveiling the coarse-scale structure of force- and stress-like objects from fine-scale flow mechanisms.

The article is organized as follows. Section 2 presents the development of the multiscale methodology employed in this work. Section 3 describes specific choices for the numerical experiments, which are presented in Section 4. Final remarks are outlined in Section 5.

2. Multiscale modeling

2.1. Hypotheses and setting

Although the framework on top of which the present model is constructed is rather general, we limit the present work by assuming the following hypotheses to hold

(H1) Two spatial scales are identified, namely a coarse and a fine scale.
(H2) Problem is steady-state.
(H3) Kinematics at coarse scale is that of a first order continuum.
(H4) Flow is incompressible at the fine scale.
(H5) Flow is single phase and Newtonian at the fine scale.
(H6) The fine scale contains rigid fixed obstacles around which the fluid flows.
(H7) No-slip conditions apply over the boundary of the obstacles.

Because of (H4) and (H6), the flow at the coarse scale is also incompressible. Removal of these hypotheses is in principle possible, but this is not a straightforward issue and requires careful modification of the multi-scale model.

2.2. Coarse-scale problem

Let us first formulate the incompressible flow problem at the coarse scale in a bounded domain $\Omega \in \mathbb{R}^n$, typically $n = 2, 3$, with boundary $\partial\Omega = \partial\Omega_D \cup \partial\Omega_N$ (D: Dirichlet, N: Neumann) with outward unit normal $\mathbf{N}$. Let us assume that the total virtual power is a linear functional only depending upon the velocity field, denoted $\mathbf{U}$, and its first gradient. Dual to these quantities there exist a vector $\mathbf{C}$ and second order tensor $\boldsymbol{\Sigma}$, that allow us to express the following: the system is at equilibrium if the following variational equation is satisfied

$$\int_\Omega \left[\mathbf{C}\cdot\hat{\mathbf{U}} + \boldsymbol{\Sigma}\cdot\nabla_\Omega\hat{\mathbf{U}}\right] d\Omega = \int_{\partial\Omega_N} \mathbf{T}\cdot\hat{\mathbf{U}}\, d\partial\Omega_N \qquad \forall\hat{\mathbf{U}} \in \mathcal{V}_\Omega, \tag{1}$$

where $\mathbf{U}$ is in a proper linear manifold $\mathcal{U}_\Omega = \{\mathbf{U} \in [H^1(\Omega)]^n,\ \mathrm{div}_\Omega\,\mathbf{U} = 0,\ \mathbf{U}|_{\partial\Omega_D} = \overline{\mathbf{U}}\}$, $\nabla_\Omega(\cdot)$ is the gradient operator with respect to coordinates $\mathbf{X} \in \Omega$, and $\mathbf{T}$ is a known datum. Besides, $\hat{(\cdot)}$ denotes admissible virtual variations in space $\mathcal{V}_\Omega$, which generates the linear manifold $\mathcal{U}_\Omega$. Also, it will be denoted $\mathbf{G} = \nabla_\Omega\mathbf{U}$, and therefore $\hat{\mathbf{G}} = \nabla_\Omega\hat{\mathbf{U}}$.

Variational equation (1) has to be supplied with closure forms for the force-like vector $\mathbf{C}$ and for the stress-like tensor $\boldsymbol{\Sigma}$. In the classical single-scale Navier-Stokes setting it is

$$\mathbf{C}_{\mathrm{NS}} = \rho(\nabla_\Omega\mathbf{U})\mathbf{U} = \rho\mathbf{G}\mathbf{U}, \tag{2}$$

$$\boldsymbol{\Sigma}_{\mathrm{NS}} = 2\mu\nabla^S_\Omega\mathbf{U} = 2\mu\mathbf{G}^S. \tag{3}$$

where ρ and μ are the density and viscosity of the fluid, respectively, $\nabla^S_\Omega(\cdot)$ is the symmetric gradient operator.

In a general setting, the variational equation (1) is closed by providing a functional form for the pair $(\mathbf{C}, \boldsymbol{\Sigma})$. These entities may depend on the velocity field $\mathbf{U}$ and on its gradient $\mathbf{G}$, that is $\mathbf{C} = \mathbf{C}(\mathbf{U}, \mathbf{G})$ and $\boldsymbol{\Sigma} = \boldsymbol{\Sigma}(\mathbf{U}, \mathbf{G})$. Note that we will allow the skew-symmetric part of the tensor $\boldsymbol{\Sigma}$ to be non-zero. Furthermore, since only divergence-free velocity fields are considered in the coarse-scale analysis, tensor $\boldsymbol{\Sigma}$ is deviatoric.

The Euler–Lagrange equations associated with Eq. (1) are derived by standard variational arguments, and, together with the essential boundary condition, they read

$$\begin{cases} \mathbf{C} - \mathrm{div}_\Omega\,\boldsymbol{\Sigma} + \nabla_\Omega P = \mathbf{0} & \text{in } \Omega, \\ \mathrm{div}_\Omega\,\mathbf{U} = 0 & \text{in } \Omega, \\ -P\mathbf{N} + \boldsymbol{\Sigma}^T\mathbf{N} = \mathbf{T} & \text{in } \partial\Omega_N, \\ \mathbf{U} = \overline{\mathbf{U}} & \text{in } \partial\Omega_D, \end{cases} \tag{4}$$

where P denotes the pressure field, which is regarded as the reaction to the divergence-free constraint considered in the space $\mathcal{V}_\Omega$. Note that, as said, by replacing (2) and (3) in (4) the steady-state Navier-Stokes equations are recovered.

Thus, the goal of the multi-scale model to be developed in the forthcoming sections is to provide Eq. (1) with closure equations for the pair $(\mathbf{C}, \boldsymbol{\Sigma})$ as a function of the pair $(\mathbf{U}, \mathbf{G})$. This is illustrated in Fig. 1, which features the basic ingredients in our multi-scale approach. For each point at the coarse scale we associate a fixed fluid Representative Volume Element (RVE, or simply cell) fixed in space, and in which the flow can have a very complex pattern due to heterogeneity of obstacles.

2.3. Kinematic coupling between scales

At the coarse scale, the kinematics have been fully characterized in Section 2.2. Recall that the fluid-velocity vector field is $\mathbf{U}$ and the velocity gradient is denoted by $\mathbf{G} = \nabla_\Omega\mathbf{U}$. These fields are defined in Ω, in which coordinates are denoted by $\mathbf{X}$.

At the fine scale, the RVE domain is denoted by $\omega \subset \mathbb{R}^n$, with boundary $\partial\omega$ (outward unit normal $\mathbf{n}$). Coordinates in ω are denoted by $\mathbf{x}$. Also, we denote by γ the boundaries of the obstacles in the fine scale.

The velocity field at the fine scale is denoted by $\mathbf{u}$. Gradient and divergence operations with respect to coordinates $\mathbf{x} \in \omega$ are denoted $\nabla_\omega(\cdot)$ and div_ω, respectively. Based on the assumptions made in Section 2.1, the velocity field at

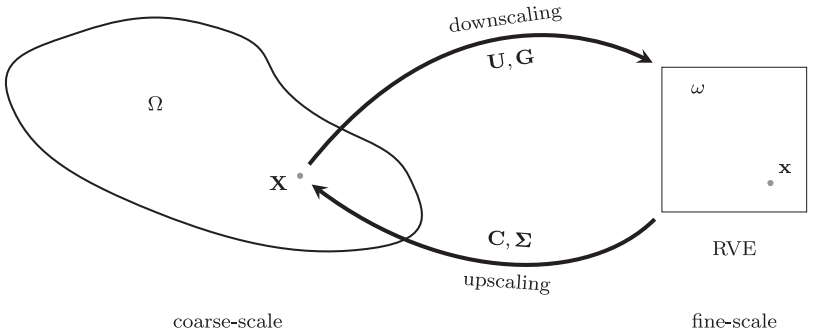

Fig. 1. Schematic coupling between coarse and fine scales. Points at the coarse scale $\mathbf{X} \in \Omega$ are coupled with RVE (coordinates $\mathbf{x} \in \omega$) that characterize the fine scale in which intricate fluid flow takes place. Downscaling kinematic variables: velocity $\mathbf{U}$ and velocity gradient $\mathbf{G}$ (see Section 2.3). Upscaling dual entities: force $\mathbf{C}$ (see Section 2.7) and stress $\boldsymbol{\Sigma}$ (see Section 2.8).

the fine scale must be divergence-free and must vanish at obstacle boundaries, that is

$$\operatorname{div}_\omega \mathbf{u} = 0 \quad \text{in } \omega, \tag{5}$$
$$\mathbf{u} = \mathbf{0} \quad \text{on } \gamma. \tag{6}$$

Fundamental to our analysis, and following the guidelines of [29], are the so-called conservation of kinematic quantities, which for the present multi-scale model they read

$$\mathbf{U} = \frac{1}{|\omega|}\int_\omega \mathbf{u}\, d\omega, \tag{7}$$
$$\mathbf{G} = \frac{1}{|\omega|}\int_\omega \nabla_\omega \mathbf{u}\, d\omega, \tag{8}$$

where $\mathbf{U}$ and $\mathbf{G}$ denote the coarse-scale fields evaluated at point $\mathbf{X}$ which is associated to ω, and $\nabla_\omega(\cdot)$ denotes the gradient operation with respect to $\mathbf{x} \in \omega$. That is, in (7) and (8) it must be understood, respectively, that

$$\mathbf{U} \in \mathbb{R}^n, \tag{9}$$
$$\mathbf{G} \in \mathbb{T}^{n\times n} = \{\mathbf{A} \in \mathbb{R}^{n\times n};\ \operatorname{tr}\mathbf{A} = 0\}. \tag{10}$$

Thus, we define the linear manifold of kinematically admissible velocity fields at fine scale as being

$$\mathcal{U}_\omega = \left\{\mathbf{u} \in [H^1(\omega)]^n,\ \mathbf{u} = \mathbf{0} \text{ on } \gamma,\ \operatorname{div}_\omega \mathbf{u} = 0,\ \frac{1}{|\omega|}\int_\omega \mathbf{u}\, d\omega = \mathbf{U},\ \frac{1}{|\omega|}\int_{\partial\omega} \mathbf{u}\otimes\mathbf{n}\, d\partial\omega = \mathbf{G}\right\}. \tag{11}$$

Introducing the variations of $\mathbf{U}$ and $\mathbf{G}$, denoted by $\hat{\mathbf{U}}$ and $\hat{\mathbf{G}}$, we have the associated space of admissible virtual variations of the velocity field

$$\mathcal{V}_\omega = \left\{\hat{\mathbf{u}} \in [H^1(\omega)]^n,\ \hat{\mathbf{u}} = \mathbf{0} \text{ on } \gamma,\ \operatorname{div}_\omega \hat{\mathbf{u}} = 0,\ \frac{1}{|\omega|}\int_\omega \hat{\mathbf{u}}\, d\omega = \hat{\mathbf{U}},\ \frac{1}{|\omega|}\int_{\partial\omega} \hat{\mathbf{u}}\otimes\mathbf{n}\, d\partial\omega = \hat{\mathbf{G}}\right\}. \tag{12}$$

It is important to remark that the linear manifold $\mathcal{U}_\omega$ (and the associated linear space $\mathcal{V}_\omega$) poses the minimum constraints to the velocity field (and its virtual variations) at the fine scale. Further assumptions on the velocity field at such scale are possible provided they are such that these constraints are met, that is, it is possible to construct a manifold such that $\mathcal{U}^*_\omega \subset \mathcal{U}_\omega$ with the corresponding space $\mathcal{V}^*_\omega \subset \mathcal{V}_\omega$, as discussed in [29]. This will be discussed in more detail when setting the numerical experiments. From now on, we continue the development with this choice of minimally constrained sets.

2.4. Mathematical duality

According to (1), the density of total virtual power at a point $\mathbf{X} \in \Omega$ in the coarse scale is a linear functional in the arguments $\hat{\mathbf{U}}$ and $\hat{\mathbf{G}}$, that is

$$\mathsf{P}_{\Omega|\mathbf{X}}(\hat{\mathbf{U}}, \hat{\mathbf{G}}) = \mathbf{C}\cdot\hat{\mathbf{U}} + \boldsymbol{\Sigma}\cdot\hat{\mathbf{G}}. \tag{13}$$

Hence, $\mathbf{C}$ is a vector dual to $\mathbf{U}$, and $\boldsymbol{\Sigma}$ is a second order tensor dual to $\mathbf{G}$.

In turn, at the fine scale, the homogenized total virtual power exerted in the RVE is

$$\mathsf{P}_\omega(\hat{\mathbf{u}}) = \frac{1}{|\omega|}\int_\omega \left[\rho(\nabla_\omega \mathbf{u})\mathbf{u}\cdot\hat{\mathbf{u}} + 2\mu\nabla^S_\omega\mathbf{u}\cdot\nabla_\omega\hat{\mathbf{u}}\right] d\omega, \tag{14}$$

where $\mathbf{u}$ is the fluid vector field at the fine scale and $\hat{\mathbf{u}}$ stand for admissible variations of such field. Here we have considered the power to be produced by viscous dissipation and convective acceleration forces. Here, μ and ρ are assumed to be constant at the fine scale.

2.5. Principle of Multiscale Virtual Power

The Principle of Multiscale Virtual Power proposed in [29] provides the physical link across scales. This principle establishes the balance between the total virtual power at the coarse scale (13) and the counterpart at the fine scale (14) performed by kinematically admissible fields, that is

$$\mathsf{P}_{\Omega|_{\mathbf{X}}}(\hat{\mathbf{U}},\hat{\mathbf{G}}) = \mathsf{P}_\omega(\hat{\mathbf{u}}) \qquad \forall \text{ kinematically admissible } \hat{\mathbf{U}},\hat{\mathbf{G}},\hat{\mathbf{u}}. \tag{15}$$

At point $\mathbf{X}$ we have $\hat{\mathbf{U}}\in\mathbb{R}^{n\times n}$ and $\hat{\mathbf{G}}\in\mathbb{T}^{n\times n}$, and the kinematic coupling between scales (kinematical admissibility) establishes that $\hat{\mathbf{u}}\in\mathcal{V}_\omega$. Thus, the statement of the principle of multi-scale virtual power results as follows.

Principle of Multiscale Virtual Power. *Given* $\mathbf{U}\in\mathbb{R}^{n\times n}$ *and* $\mathbf{G}\in\mathbb{T}^{n\times n}$*, it is said that* $\mathbf{C}$*,* $\boldsymbol{\Sigma}$ *and* $\mathbf{u}\in\mathcal{U}_\omega$ *satisfy the Principle of Multiscale Virtual Power if the following variational equation holds*

$$\mathbf{C}\cdot\hat{\mathbf{U}} + \boldsymbol{\Sigma}\cdot\hat{\mathbf{G}} = \frac{1}{|\omega|}\int_\omega \left[\rho(\nabla_\omega\mathbf{u})\mathbf{u}\cdot\hat{\mathbf{u}} + 2\mu\nabla^S_\omega\mathbf{u}\cdot\nabla_\omega\hat{\mathbf{u}}\right] d\omega \quad \forall(\hat{\mathbf{U}},\hat{\mathbf{G}},\hat{\mathbf{u}})\in\mathbb{R}^n\times\mathbb{T}^{n\times n}\times\mathcal{V}_\omega. \quad \blacksquare \tag{16}$$

Now, the variational formulation (16) is rewritten using Lagrange multipliers to remove kinematical constraints present in the linear manifold $\mathcal{U}_\omega$ (see (11)). That is, consider the following Lagrange multipliers

- $\mathbf{r}\in[H^{-1/2}(\gamma)]^n$ (obstacle forces) associated to the constraint $\mathbf{u}=\mathbf{0}$ on γ,
- $p\in L^2(\omega)$ (pressure) associated to the constraint $\operatorname{div}_\omega\mathbf{u}=0$ in ω,
- $\boldsymbol{\lambda}\in\mathbb{R}^n$ associated to the constraint $\frac{1}{|\omega|}\int_\omega\mathbf{u}\,d\omega=\mathbf{U}$,
- $\boldsymbol{\Lambda}\in\mathbb{T}^{n\times n}$ associated to the constraint $\frac{1}{|\omega|}\int_{\partial\omega}\mathbf{u}\otimes\mathbf{n}\,d\partial\omega=\mathbf{G}$.

Then, the variational formulation can equivalently be written as follows using Lagrange multipliers.

Principle of Multiscale Virtual Power (Lagrange multipliers). *Given* $\mathbf{U}\in\mathbb{R}^{n\times n}$ *and* $\mathbf{G}\in\mathbb{T}^{n\times n}$*, it is said that* $\mathbf{C}$*,* $\boldsymbol{\Sigma}$ *and* $\mathbf{u}\in[H^1(\omega)]^n$ *satisfy the Principle of Multiscale Virtual Power if the following variational equation holds*

$$\begin{aligned}
\mathbf{C}\cdot\hat{\mathbf{U}} + \boldsymbol{\Sigma}\cdot\hat{\mathbf{G}} \;=\; & \frac{1}{|\omega|}\Bigg\{\int_\omega\left[\rho(\nabla_\omega\mathbf{u})\mathbf{u}\cdot\hat{\mathbf{u}} + 2\mu\nabla^S_\omega\mathbf{u}\cdot\nabla_\omega\hat{\mathbf{u}}\right]d\omega \\
& + \int_\gamma \mathbf{r}\cdot\hat{\mathbf{u}}\,d\gamma + \int_\gamma\hat{\mathbf{r}}\cdot\mathbf{u}\,d\gamma - \int_\omega p\operatorname{div}_\omega\hat{\mathbf{u}}\,d\omega - \int_\omega\hat{p}\operatorname{div}_\omega\mathbf{u}\,d\omega \\
& + \hat{\boldsymbol{\lambda}}\cdot\left[\mathbf{U}-\frac{1}{|\omega|}\int_\omega\mathbf{u}\,d\omega\right] + \boldsymbol{\lambda}\cdot\left[\hat{\mathbf{U}}-\frac{1}{|\omega|}\int_\omega\hat{\mathbf{u}}\,d\omega\right] \\
& + \hat{\boldsymbol{\Lambda}}\cdot\left[\mathbf{G}-\frac{1}{|\omega|}\int_{\partial\omega}\mathbf{u}\otimes\mathbf{n}\,d\partial\omega\right] + \boldsymbol{\Lambda}\cdot\left[\hat{\mathbf{G}}-\frac{1}{|\omega|}\int_{\partial\omega}\hat{\mathbf{u}}\otimes\mathbf{n}\,d\partial\omega\right]\Bigg\} \\
\forall(\hat{\mathbf{U}},\hat{\mathbf{G}},\hat{\mathbf{u}})\in\mathbb{R}^n\times\mathbb{T}^{n\times n}\times[H^1(\omega)]^n\;\forall(\hat{\boldsymbol{\lambda}},\hat{\boldsymbol{\Lambda}},\hat{p},\hat{\mathbf{r}})\in\mathbb{R}^n\times\mathbb{T}^{n\times n}\times L^2(\omega)\times[H^{-1/2}(\gamma)]^n. & \quad \blacksquare
\end{aligned} \tag{17}$$

The Euler–Lagrange equations corresponding to the variational problem (17) are derived in the forthcoming sections.

2.6. Fine-scale problem

Consider $\hat{\mathbf{U}} = \mathbf{0}$ and $\hat{\mathbf{G}} = \mathbf{0}$ in (17). Then, the equilibrium problem at the fine scale is defined by the following variational formulation: given $\mathbf{U} \in \mathbb{R}^n$ and $\mathbf{G} \in \mathbb{T}^{n\times n}$, find $(\mathbf{u}, \boldsymbol{\lambda}, \boldsymbol{\Lambda}, \mathbf{r}, p) \in [H^1(\omega)]^n \times \mathbb{R}^n \times \mathbb{T}^{n\times n} \times [H^{-1/2}(\gamma)]^n \times L^2(\omega)$ such that

$$
\begin{aligned}
&\int_\omega \left[\rho(\nabla_\omega \mathbf{u})\mathbf{u}\cdot\hat{\mathbf{u}} + 2\mu\nabla^S_\omega\mathbf{u}\cdot\nabla_\omega\hat{\mathbf{u}} - p\,\mathrm{div}_\omega\,\hat{\mathbf{u}} - \hat{p}\,\mathrm{div}_\omega\,\mathbf{u} - \tfrac{1}{|\omega|}\boldsymbol{\lambda}\cdot\hat{\mathbf{u}}\right] d\omega \\
&\quad + \int_\gamma \left[\mathbf{r}\cdot\hat{\mathbf{u}} + \hat{\mathbf{r}}\cdot\mathbf{u}\right] d\gamma - \int_{\partial\omega} \tfrac{1}{|\omega|}\boldsymbol{\Lambda}\mathbf{n}\cdot\hat{\mathbf{u}}\, d\partial\omega \\
&\quad + \hat{\boldsymbol{\lambda}}\cdot\left[\mathbf{U} - \frac{1}{|\omega|}\int_\omega \mathbf{u}\, d\omega\right] + \hat{\boldsymbol{\Lambda}}\cdot\left[\mathbf{G} - \frac{1}{|\omega|}\int_{\partial\omega}\mathbf{u}\otimes\mathbf{n}\, d\partial\omega\right] = 0 \\
&\quad \forall(\hat{\mathbf{u}}, \hat{\boldsymbol{\lambda}}, \hat{\boldsymbol{\Lambda}}, \hat{p}, \hat{\mathbf{r}}) \in [H^1(\omega)]^n \times \mathbb{R}^n \times \mathbb{T}^{n\times n} \times L^2(\omega) \times [H^{-1/2}(\gamma)]^n.
\end{aligned}
\tag{18}
$$

Using standard variational arguments, we obtain the associated set of partial differential equations for the problem in the fine-scale

$$
\begin{cases}
\rho(\nabla_\omega\mathbf{u})\mathbf{u} - \mu\Delta_\omega\mathbf{u} + \nabla_\omega p = \dfrac{1}{|\omega|}\boldsymbol{\lambda} & \text{in } \omega \\
\mathrm{div}_\omega\,\mathbf{u} = 0 & \text{in } \omega, \\
\mathbf{u} = \mathbf{0} & \text{on } \gamma, \\
(-p\mathbf{I} + 2\mu\nabla^S_\omega\mathbf{u})\mathbf{n} = -\mathbf{r} & \text{on } \gamma, \\
\dfrac{1}{|\omega|}\displaystyle\int_\omega \mathbf{u}\, d\omega = \mathbf{U}, & \\
\dfrac{1}{|\omega|}\displaystyle\int_{\partial\omega}\mathbf{u}\otimes\mathbf{n}\, d\partial\omega = \mathbf{G}, & \\
(-p\mathbf{I} + 2\mu\nabla^S_\omega\mathbf{u})\mathbf{n} = \dfrac{1}{|\omega|}\boldsymbol{\Lambda}\mathbf{n} & \text{on } \partial\omega.
\end{cases}
\tag{19}
$$

From a control perspective, $\boldsymbol{\lambda}$ is a force term per unit volume that controls that constraint $\frac{1}{|\omega|}\int_\omega \mathbf{u}\, d\omega = \mathbf{U}$ holds, while $\boldsymbol{\Lambda}\mathbf{n}$ is a force term per unit surface that controls that constraint $\frac{1}{|\omega|}\int_{\partial\omega}\mathbf{u}\otimes\mathbf{n}\, d\partial\omega = \mathbf{G}$ is also satisfied.

2.7. Force-like vector homogenization

Now, consider non-zero variations of $\tilde{\mathbf{U}}$ only in (17), which yields

$$
\mathbf{C} = \boldsymbol{\lambda}, \tag{20}
$$

which implies that the coarse scale force $\mathbf{C} \in \mathbb{R}^n$ is balanced by the reactive force that controls the averaged velocity at the fine scale.

For this choice of $\mathcal{U}_\omega$ and $\mathcal{V}_\omega$, it can be shown (see Appendix) that the following expression holds in terms of the fine scale fields $\mathbf{u}$ and $\mathbf{r}$

$$
\mathbf{C} = \frac{1}{|\omega|}\left[\int_\omega \rho(\nabla_\omega\mathbf{u})\mathbf{u}\, d\omega + \int_\gamma \mathbf{r}\, d\gamma\right]. \tag{21}
$$

The first term in (21) comprises the classical convective force in the Navier-Stokes equations (see (2)) incremented with higher order terms, and the second term represents the classical Darcy term observed in porous media models, in which a volume force appears as a result of the resistance to flow imposed by obstacles.

2.8. Stress-like tensor homogenization

In (17) consider now that just $\hat{\mathbf{G}} \neq \mathbf{0}$. This results in

$$
\boldsymbol{\Sigma} = \boldsymbol{\Lambda}, \tag{22}
$$

that is, the coarse scale stress tensor $\boldsymbol{\Sigma}$ is equal to the reactive force that controls the averaged velocity gradient at the fine scale. Clearly, since $\mathbf{G} \in \mathbb{T}^{n\times n}$, it results $\boldsymbol{\Sigma} \in \mathbb{T}^{n\times n}$.

For this choice of $\mathcal{U}_\omega$ and $\mathcal{V}_\omega$, it can be shown (see Appendix) that the following characterization holds in terms of the fine scale velocity field $\mathbf{u}$ and of the Lagrange multiplier $\mathbf{r}$

$$\boldsymbol{\Sigma} = \frac{1}{|\omega|}\left[\int_\omega \left[\rho(\nabla_\omega \mathbf{u})\mathbf{u}\otimes\mathbf{x} + 2\mu\nabla^S_\omega \mathbf{u}\right] d\omega + \int_\gamma \mathbf{r}\otimes\mathbf{x}\, d\gamma\right]^D, \tag{23}$$

where $(\cdot)^D = (\cdot) - \frac{1}{3}\,\mathrm{tr}(\cdot)\mathbf{I}$, with $\mathbf{I}$ the second order identity tensor, denotes the deviatoric projection.

The first term in (23) contains high order moments of the forces associated to the convective acceleration, the second term contains the classical viscous stress in the Navier-Stokes model (see (3)) plus additional higher order terms because of the non-homogeneous gradient. Finally, the third term describes the moment produced by obstacle forces.

3. Numerical setting

3.1. Boundary conditions

In this section we present the method used to construct boundary conditions for the multi-scale simulations presented in this work. In principle, any boundary conditions that comply with the kinematic restrictions (7) and (8) are valid. For example, the microscale velocity field can be decomposed as $\mathbf{u} = \mathbf{U} + \mathbf{G}\mathbf{x} + \tilde{\mathbf{u}}$, and periodic conditions can be imposed on $\tilde{\mathbf{u}}$. However, periodic conditions for the fluctuation field $\tilde{\mathbf{u}}$ may not be appropriate to model non-periodic micro-structures and may overconstrain physical phenomena. This motivates the development of an intermediate boundary condition as explained next.

The proposed boundary condition makes use of an extension of the fluid domain ω, by adding a frame, say ω_f whose interface with ω is $\partial\omega$ and the external boundary is called $\partial\omega_f$. This is represented by the gray filled area shown in Fig. 2. The extended RVE is denoted by $\omega_e = \omega \cup \omega_f$. Then, the chosen linear manifold $\mathcal{U}^*_\omega \subset \mathcal{U}_\omega$ and its associated linear space $\mathcal{V}^*_\omega \subset \mathcal{V}_\omega$ are such that

$$\mathcal{U}^*_\omega = \{\mathbf{u}\in\mathcal{U}_\omega,\ \mathbf{u} = \mathbf{u}_e|_\omega,\ \mathbf{u}_e \in [H^1(\omega_e)]^n,\ \mathbf{u}_e|_{\partial\omega_f} \text{ satisfies b.c.}\}, \tag{24}$$

and

$$\mathcal{V}^*_\omega = \{\mathbf{v}\in\mathcal{V}_\omega,\ \mathbf{v} = \mathbf{v}_e|_\omega,\ \mathbf{v}_e \in [H^1(\omega_e)]^n,\ \mathbf{v}_e|_{\partial\omega_f} \text{ satisfies b.c.}\}. \tag{25}$$

With such construction, and recalling that the restriction of $\mathbf{u}_e$ to ω is $\mathbf{u}$, the set of partial differential equations (19) becomes

$$\begin{cases} \rho(\nabla_\omega \mathbf{u})\mathbf{u} - \mu\Delta_\omega \mathbf{u} + \nabla_\omega p = \dfrac{1}{|\omega|}\boldsymbol{\lambda} & \text{in } \omega \\ \rho(\nabla_\omega \mathbf{u}_e)\mathbf{u}_e - \mu\Delta_\omega \mathbf{u}_e + \nabla_\omega p_e = \mathbf{0} & \text{in } \omega_f \\ \mathrm{div}_\omega\, \mathbf{u} = 0 & \text{in } \omega, \\ \mathrm{div}_\omega\, \mathbf{u}_e = 0 & \text{in } \omega_f, \\ \mathbf{u} = \mathbf{0} & \text{on } \gamma, \\ (-p\mathbf{I} + 2\mu\nabla^S_\omega \mathbf{u})\mathbf{n} = -\mathbf{r} & \text{on } \gamma, \\ \dfrac{1}{|\omega|}\displaystyle\int_\omega \mathbf{u}\, d\omega = \mathbf{U}, & \\ \dfrac{1}{|\omega|}\displaystyle\int_{\partial\omega} \mathbf{u}\otimes\mathbf{n}\, d\partial\omega = \mathbf{G}, & \\ [\![(-p\mathbf{I} + 2\mu\nabla^S_\omega \mathbf{u})\mathbf{n}]\!] = \dfrac{1}{|\omega|}\boldsymbol{\Lambda}\mathbf{n} & \text{on } \partial\omega, \\ \mathbf{u}_e \text{ satisfies b.c.} & \text{on } \partial\omega_f, \end{cases} \tag{26}$$

where $[\![\cdot]\!]$ indicates the jump of the quantity $(\cdot)$ across the boundary $\partial\omega$. Notice that this is a model in which the traction vector over the RVE boundary $\partial\omega$ is not uniform (the traction jump is in fact a uniform quantity).

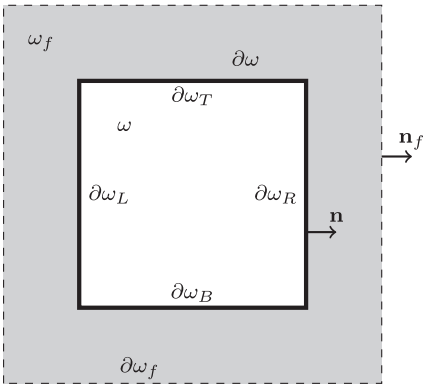

Fig. 2. Extension of RVE domain ω through the addition of a frame domain ω_f represented by the gray area. The solid line represents the physical boundary of the RVE, called $\partial\omega = \partial\omega_T \cup \partial\omega_R \cup \partial\omega_B \cup \partial\omega_L$ (outward normal $\mathbf{n}$), while the dashed line represents the external boundary of the frame domain, called $\partial\omega_f$ (outward normal $\mathbf{n}_f$). The extended RVE domain is denoted by $\omega_e = \omega \cup \omega_f$.

Remarkably, the RVE is less sensitive to the setting of boundary conditions because the external boundary of the extended RVE $\partial\omega_f$ is far from the actual RVE domain in which the fine scale dynamics is being linked to the coarse scale model. In contrast, the fine scale problem is more expensive to solve because of the larger domain. The boundary condition over $\partial\omega_f$ is defined in next section.

3.2. Numerical method

The fine scale problem (26) for $n = 2$ is numerically solved using the Lattice–Boltzmann method (LBM) to take advantage of its versatility to handle constraints through the imposition of volume and boundary forces. This has shown excellent performance in the simulation of flow amid obstacles [35]. Because of the explicit nature of the LBM, a pseudo-transient problem (pseudo-time denoted by t) is solved until the steady-state is reached. Accordingly, a rectangular RVE is represented by a regular grid of square cells and the state of the cell at point $\mathbf{x}$ and time t is given by nine scalars $f_i(\mathbf{x}, t)$ associated to nine grid directions $\mathbf{e}_i$ (i: 1–4 Cartesian, 5–8 diagonal, 0 null velocity). The governing equation for each f_i is given by

$$f_i(\mathbf{x} + \mathbf{e}_i \Delta x, t + \Delta t) = f_i(\mathbf{x}, t) + \frac{f_i^e(\mathbf{x}, t) - f_i(\mathbf{x}, t)}{\tau} + S_i(\mathbf{x}, t), \tag{27}$$

from which it is defined $v = \frac{\Delta x}{\Delta t}$, called the grid velocity.

The chosen equilibrium function $f_i^e(\mathbf{x}, t)$ is the quasi-incompressible BGK D2Q9 scheme proposed by [36], which leads to the Navier-Stokes equations in the differential limit and keeps the divergence as low as possible, that is

$$f_i^e(\mathbf{x}, t) = w_i \left[\rho^* + \rho \left(3 \frac{(v\mathbf{e}_i \cdot \mathbf{u})}{v^2} - \frac{3}{2} \frac{\mathbf{u} \cdot \mathbf{u}}{v^2} + \frac{9}{2} \frac{(v\mathbf{e}_i \cdot \mathbf{u})^2}{v^4} \right) \right] \tag{28}$$

with $w_i = \frac{4}{9}$ for $i = 0$, $w_i = \frac{1}{9}$ for $i = 1, 2, 3, 4$ and $w_i = \frac{1}{36}$ for $i = 5, 6, 7, 8$,

$$\rho^*(\mathbf{x}, t) = \sum_{i=0}^{8} f_i(\mathbf{x}, t) \qquad \mathbf{u}(\mathbf{x}, t) = \frac{v}{\rho} \sum_{i=0}^{8} f_i(\mathbf{x}, t) \mathbf{e}_i, \tag{29}$$

and ρ is the mean density. In the LBM the kinematic viscosity $\nu = \frac{\mu}{\rho}$ is given by

$$\nu = \frac{1}{3} \left(\tau - \frac{1}{2} \right) \frac{\Delta x^2}{\Delta t}. \tag{30}$$

The source term S_i in Eq. (27) accounts in general for external forces. There are several schemes to take into account forces that can be applied. Here, the formula suggested by [37] is employed, which showed accuracy and stability in

simulations of permeable media [35]. Accordingly, an external force field $\mathbf{F}(\mathbf{x}, t)$ introduces a source term

$$S_i(\mathbf{x}, t) = \frac{\Delta t}{3v} w_i \mathbf{e}_i \cdot \mathbf{F}(\mathbf{x}, t). \tag{31}$$

It is straightforward to verify that

$$\sum_{i=0}^{8} S_i(\mathbf{x}, t) = 0 \qquad \sum_{i=0}^{8} v\mathbf{e}_i S_i(\mathbf{x}, t) = \mathbf{F}(\mathbf{x}, t)\Delta t, \tag{32}$$

providing the bit of impulse at each time step without perturbing the mass balance.

The calculation of the fine scale field $\mathbf{u}$ inside the RVE has to be performed under the constraints given by Eqs. (26)$_7$ and (26)$_8$, which requires the imposition of forces acting as Lagrange multipliers, called $\boldsymbol{\lambda}$ and $\boldsymbol{\Lambda}\mathbf{n}$, see (26)$_1$ and (26)$_9$. Likewise, the no-slip conditions over the boundaries of the internal objects γ, see (26)$_5$, entail the imposition of the reaction forces $\mathbf{r}$, see (26)$_6$. In order to determine the forces $\frac{1}{|\omega|}\boldsymbol{\lambda}$, $\frac{1}{|\omega|}\boldsymbol{\Lambda}\mathbf{n}$ and $\mathbf{r}$, a model of classical adaptive proportional–integral control is included, which responds to deviations from each restriction. Accordingly, at every time t the deviation $\boldsymbol{\varepsilon}(t)$ from a given constraint is calculated, and the corrective force is then calculated as

$$\mathbf{F}(t) = \alpha\boldsymbol{\varepsilon}(t) + \beta \sum_{s=0}^{t} \boldsymbol{\varepsilon}(s), \tag{33}$$

where α and β are appropriate control coefficients that should be adjusted to ensure stable and rapid feedback, and are force-specific. In all the calculations shown in the next section, α and β were set in $1 \cdot 10^{-6}$ and $5 \cdot 10^{-9}$. In this way, when the flow reaches the steady state, the residual accumulated in last term corresponds to the force that is necessary to maintain the corresponding constraint. Actually, this force model can be seen as a sort of predictor–corrector algorithm with relaxation. In particular, the following deviations are implemented to control the average velocity (26)$_7$, the average gradient (26)$_8$ and the velocity at the internal boundaries (26)$_5$, respectively

$$\boldsymbol{\varepsilon}_{\boldsymbol{\lambda}} = \mathbf{U} - \frac{1}{|\omega|}\int_{\omega} \mathbf{u}(\mathbf{x}, t)\, d\omega, \tag{34}$$

$$\boldsymbol{\varepsilon}_{\boldsymbol{\Lambda}} = \mathbf{G} - \frac{1}{|\omega|}\int_{\partial\omega} \mathbf{u}(\mathbf{x}, t) \otimes \mathbf{n}(\mathbf{x})\, d\partial\omega, \tag{35}$$

$$\boldsymbol{\varepsilon}_{\mathbf{r}} = -\mathbf{u}(\mathbf{x}, t) \qquad \mathbf{x} \in \gamma. \tag{36}$$

The force per unit volume $\frac{1}{|\omega|}\boldsymbol{\lambda}$ is imposed uniformly on each point $\mathbf{x}$ corresponding to the interior of the RVE ω. The surface force of the obstacles $\mathbf{r}$ is imposed on every point $\mathbf{x} \in \gamma$. The surface force $\frac{1}{|\omega|}\boldsymbol{\Lambda}\mathbf{n}$ is imposed uniformly at each side of the RVE boundary $\partial\omega$. In Cartesian coordinates ($\mathbf{e}_x$ and $\mathbf{e}_y$ the unit vectors in x and y directions), we can rewrite the deviation (35) which guide the computation of the force $\frac{1}{|\omega|}\boldsymbol{\Lambda}\mathbf{n}$ as follows

$$\boldsymbol{\varepsilon}^T_{\boldsymbol{\Lambda}} = -\boldsymbol{\varepsilon}^B_{\boldsymbol{\Lambda}} = \mathbf{G} \cdot \mathbf{e}_y - \frac{1}{|\omega|}\left[\int_{\partial\omega_T} \mathbf{u}(\mathbf{x}, t)\, d\partial\omega_T - \int_{\partial\omega_B} \mathbf{u}(\mathbf{x}, t)\, d\partial\omega_B\right], \tag{37}$$

$$\boldsymbol{\varepsilon}^R_{\boldsymbol{\Lambda}} = -\boldsymbol{\varepsilon}^L_{\boldsymbol{\Lambda}} = \mathbf{G} \cdot \mathbf{e}_x - \frac{1}{|\omega|}\left[\int_{\partial\omega_R} \mathbf{u}(\mathbf{x}, t)\, d\partial\omega_R - \int_{\partial\omega_L} \mathbf{u}(\mathbf{x}, t)\, d\partial\omega_L\right], \tag{38}$$

where the different boundaries of the rectangular RVE were identified $\partial\omega_T$ (top), $\partial\omega_B$ (bottom), $\partial\omega_R$ (right) and $\partial\omega_L$ (left). These boundaries are also identified in Fig. 2. In the 2D Cartesian reference frame, $\boldsymbol{\varepsilon}^T_{\boldsymbol{\Lambda}}$ and $\boldsymbol{\varepsilon}^R_{\boldsymbol{\Lambda}}$ are, respectively, the first and second rows of tensor $\boldsymbol{\varepsilon}_{\boldsymbol{\Lambda}}$ defined in (35).

For the LBM to be fully closed it is necessary to provide the set of boundary conditions for all the scalar fields $f_i(\mathbf{x}, t)$ over the boundary $\partial\omega_f$ of the extended RVE domain. At $\partial\omega_f$, periodic boundary conditions for all fields $f_i(\mathbf{x}, t)$ are imposed. With this choice, $\mathcal{U}^*_\omega$ and $\mathcal{V}^*_\omega$ are fully characterized and the problem is closed.

As already said, all test cases that will be addressed in the next section are in the steady-state regime. Therefore the time-dependent Lattice–Boltzmann problem is solved until the steady state is reached.

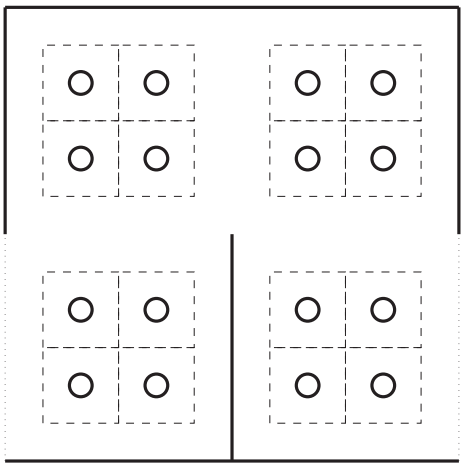

Fig. 3. Diagram of the geometrical configuration chosen for benchmarking the present methodology in a fully controlled case. The side of the RVE is 5 times larger than the radius of the obstacle. Dashed lines indicate the 16 RVEs used in the calculation of homogenized quantities. Periodic boundary conditions are imposed over dotted boundaries.

Finally, observe that by solving (26) with the proposed approach we are obtaining the Lagrange multipliers $\boldsymbol{\lambda}$ and $\boldsymbol{\Lambda}$ as feedback forces of the proportional–integral controller. However, the computation of homogenized quantities $\mathbf{C}$ and $\boldsymbol{\Sigma}$ is carried out using (21) and (23), respectively.

4. Numerical experiments

Firstly, in Section 4.1 a test of consistency is performed on a geometry where a variety of kinematic conditions of mean velocity and velocity gradient occur. Secondly, the homogeneous magnitudes of a typical RVE subjected to fully-developed flow conditions were calculated and analyzed in Section 4.2. Finally, the solution delivered by the multi-scale model is validated by comparison against a solution obtained by direct numerical simulation (DNS) in Section 4.3.

4.1. Consistency test

The first case consists of a squared channel with a buffer located at mid run to divert the bulk stream, as seen in Fig. 3. Periodic boundary conditions are imposed between the inlet and the outlet. Hence, the problem can be seen as a section of a long rectangular channel with alternate upper and lower buffers. An array of circular obstacles was located inside the channel, from which the flow experiences a variety of velocity $\mathbf{U}$ and velocity gradient $\mathbf{G}$ conditions. The complete channel with all the complexity was solved by DNS using also the LBM, obtaining the velocity field in steady state amid the obstacles.

Fig. 4 shows the contour maps of the components of the velocity field in the channel. The horizontal component, U_X, is larger along a stream of minimum path joining the upper part of each opening passing around the tip of the buffer. In turn, on either side of the buffer there are regions of high upward and downward vertical velocity U_Y. Both fields are also perturbed by the presence of the circular obstacles.

The channel is then divided into 16 square RVEs containing one obstacle each in its center (see Fig. 3). The velocity and its gradient obtained by DNS are then averaged in each RVE, leading to a set of 16 coarse scale flow conditions given by the vector–tensor pairs $(\mathbf{U}_{\mathrm{DNS}}, \mathbf{G}_{\mathrm{DNS}})$. Each of these conditions is then applied as coarse-scale data to the solution of the fine-scale problem of a single RVE cell (which is surrounded by a peripheral frame ω_f with periodic boundaries, as described in the previous section), to obtain the homogenized quantities that will be referred to as $\mathbf{C}_{\mathrm{RVE}}$ and $\boldsymbol{\Sigma}_{\mathrm{RVE}}$. These quantities are then compared with the true values, $\mathbf{C}_{\mathrm{DNS}}$ and $\boldsymbol{\Sigma}_{\mathrm{DNS}}$, which are computed by applying (21) and (23) to the DNS field in the corresponding region of the channel.

Fig. 5 shows the plot of the true (DNS) vs. multi-scale (RVE) components of the force $\mathbf{C} = (C_X, C_Y)$ and of the stress $\boldsymbol{\Sigma} = \begin{pmatrix} \Sigma_{XX} & \Sigma_{XY} \\ \Sigma_{YX} & \Sigma_{YY} \end{pmatrix}$, discriminating the symbols by terms and directions in order to appraise the agreement in

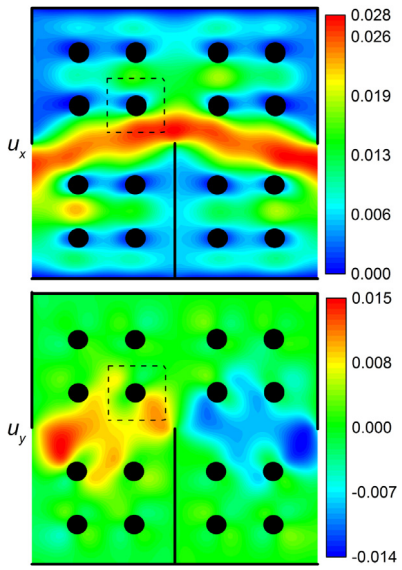

Fig. 4. Magnitude of the components U_X (top) and U_Y (bottom) of the velocity field.

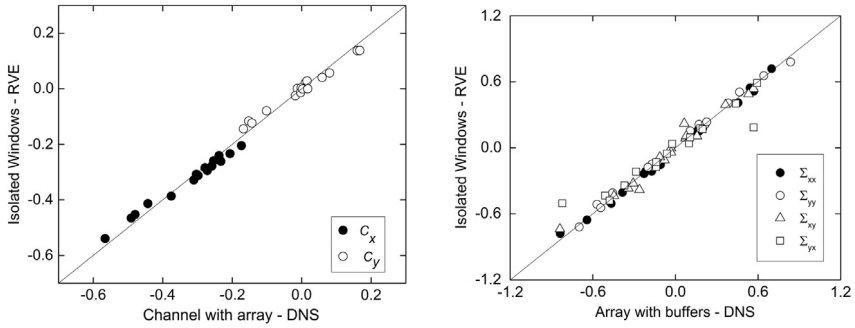

Fig. 5. Comparison of the components of homogenized quantities $\mathbf{C} = (C_X, C_Y)$ (left) and $\boldsymbol{\Sigma} = \begin{pmatrix} \Sigma_{XX} & \Sigma_{XY} \\ \Sigma_{YX} & \Sigma_{YY} \end{pmatrix}$ (right) from fine scale computations performed at the RVE with corresponding flow conditions given by $(\mathbf{U}_{\text{DNS}}, \mathbf{G}_{\text{DNS}})$ against the homogenization of the results delivered by the DNS.

each case. The ideal situation occurs when the points lie on the 45 degree line. Remarkably, the correlation between the DNS calculations and the approximations obtained with the present multi-scale methodology is strong, which provides convincing evidences of the predictive capabilities of the homogenization procedure. That is, the multi-scale approach proposed in this work is capable of retrieving most of the physics present in the original fine scale problem. To further verify and illustrate this statement, Fig. 6 compares the flow field obtained from the DNS and the RVE for the window indicated with dashed lines in Fig. 4. It is remarkable that the flow patterns computed in the RVE are very close to the ones obtained from the DNS case, even in the present case where separation of scales is not guaranteed.

4.2. Homogenized parameters of a RVE in fully developed flow

The second problem studied was the influence of the coarse scale flow conditions $(\mathbf{U}, \mathbf{G})$ on the homogenized quantities $(\mathbf{C}, \boldsymbol{\Sigma})$ through the solution of the fine scale problem in a flow fully developed in the X direction. These conditions would be expected for instance in a long rectangular channel filled with a regular array of obstacles (see the validation against DNS calculations in Section 4.3). The square RVE that characterizes this problem was modeled by a grid of side $L_{\text{RVE}} = 100$ cells, and contains two semicircular cylinders of radius $R = \frac{L_{\text{RVE}}}{20}$, centered at the midpoint of the upper and lower borders. The density ρ and the relaxation parameter τ were fixed in 0.009 and 0.55 (in grid units), respectively. Since the flow is fully developed it is $U_Y = 0$, and U_X depends only on the coordinate

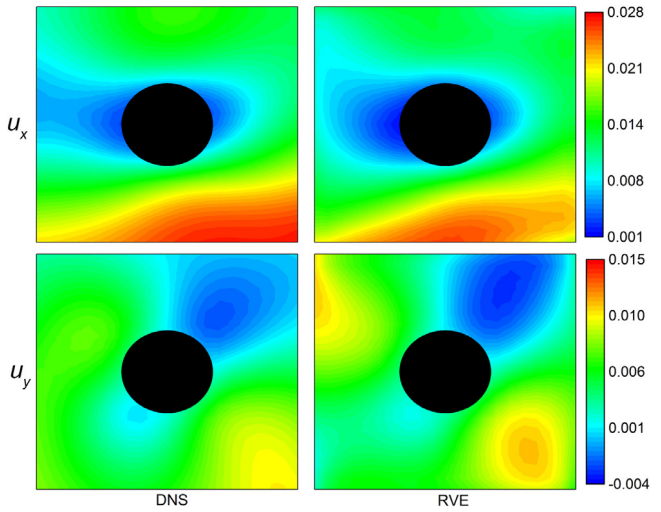

Fig. 6. Comparison of velocity magnitudes U_X and U_Y in the RVE domain corresponding to the dashed window shown in Fig. 4 between the fine scale computations at the RVE (with corresponding flow conditions ($\mathbf{U}_{\text{DNS}}$, $\mathbf{G}_{\text{DNS}}$) and the results rendered by DNS).

Y. Therefore, the coarse-scale state of any RVE is determined only by U_X and G_{XY}. Different kinematic conditions, U_X and G_{XY}, are imposed upon the RVE, covering a range of Reynolds numbers ($\text{Re} = \frac{U_X L_{\text{RVE}}}{\nu}$) from 0 to 30, and a range of the dimensionless gradient $\text{Gd} = \frac{G_{XY} L_{\text{RVE}}^2}{\nu}$ (from now on called *Gradient number*) from 0 to 60.

For generality, it is convenient to express the coarse magnitudes C_X and Σ_{XY} in dimensionless units, that is

$$\tilde{C}_X = \frac{C_X L_{\text{RVE}}^3}{\rho \nu^2}, \tag{39}$$

$$\tilde{\Sigma}_{XY} = \frac{\Sigma_{XY} L_{\text{RVE}}^2}{\rho \nu^2}. \tag{40}$$

Fig. 7 (left) shows the magnitude and direction of the velocity field (top), $\mathbf{u}$, and of the acceleration force (bottom), $\rho(\nabla_\omega \mathbf{u})\mathbf{u}$, computed in the RVE subjected to the coarse scale flow conditions given by $U_X = 0.001$ and $G_{XY} = 0$ (in grid units). The latter corresponds to $\text{Re} = 6$. The velocity field is symmetric with respect to the horizontal axis, where it reaches the maximum velocity due to the reduction of the cross sectional area. The acceleration force is also axially symmetric and presents maxima in the neighborhoods of the obstacles and a minimum at the axis. Fig. 7 (right) shows the same fields for coarse scale flow conditions established by $U_X = 0.001$ and $G_{XY} = 5 \cdot 10^{-6}$ (in grid units), corresponding to $\text{Re} = 6$ and $\text{Gd} = 3$. The positive gradient G_{XY} induces the symmetry breaking observed in both fields.

Fig. 8 (left) shows the dependence of the homogenized magnitude C_X with U_X in dimensionless units. For the range of Gd analyzed, C_X resulted independent of G_{XY}. If the Darcy law was supposed to govern the relation between C_X and U_X, it would be $C_X = \frac{\mu}{\kappa} U_X$. The permeability κ is a geometrical property of the media with units of square length. In dimensionless magnitudes, we have $\tilde{C}_X = \frac{L_{\text{RVE}}^2}{\kappa}\text{Re}$, which in the present case gives $\frac{\kappa}{L_{\text{RVE}}^2} = 0.083$.

Fig. 8 (right) shows the dependence of the coarse-scale stress component Σ_{XY} with G_{XY} in dimensionless units. For the range of Re analyzed Σ_{XY} resulted independent of U_X. Since the fluid is Newtonian, in the absence of obstacles the stress should be $\Sigma_{XY} = \mu G_{XY}$ (in fully developed flow), which in dimensionless form gives $\tilde{\Sigma}_{XY} = \text{Gd}$. Hence, the derivative of $\tilde{\Sigma}_{XY}$ with respect to Gd represents the deviation from the homogeneous Newtonian behavior, and it is interpreted as an effective viscosity $\tilde{\mu}_e = \frac{\mu_e}{\mu}$ at coarse scale, resulting from the viscous interaction between the flow and the obstacle at the fine scale, namely, $\tilde{\Sigma}_{XY} = \tilde{\mu}_e \text{Gd}$. For the present case the effective viscosity resulted $\tilde{\mu}_e = 6.9$, which is consistent with experimental measurements performed in permeable media with similar void fractions and Re numbers [38]. The main contribution to the effective viscosity comes from $\frac{1}{|\omega|}\int_\gamma r_x y \, d\gamma$ (XY component of the

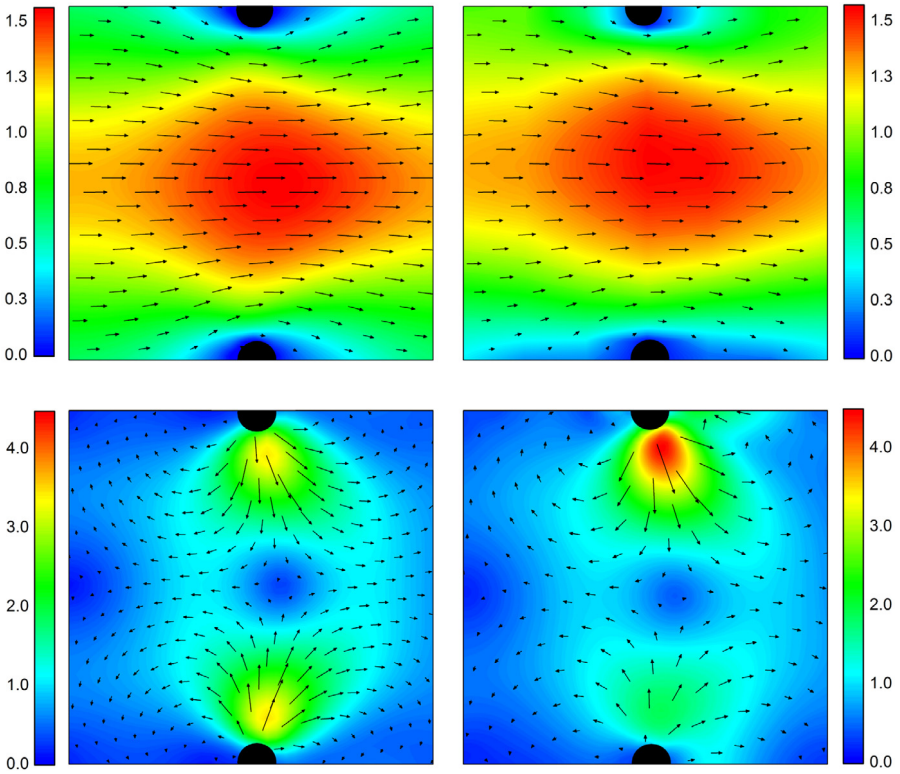

Fig. 7. Velocity $\mathbf{u}$ (top row) and convective acceleration $\rho(\nabla_\omega \mathbf{u})\mathbf{u}$ (bottom row) in the RVE. Flow conditions are given by: (Re, Gd) = (6, 0) (left column) and (Re, Gd) = (6, 3) (right column). Color scale indicates the magnitude of the field normalized by the mean value.

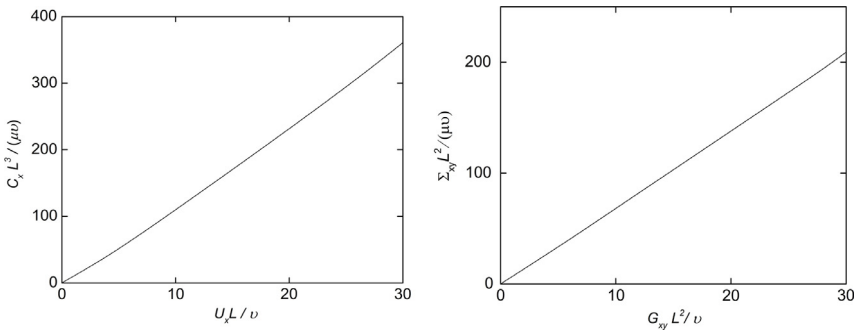

Fig. 8. Left panel shows the dependence of the force C_X with the coarse scale velocity U_X. Right panel features the dependence of the stress Σ_{XY} with the coarse scale gradient G_{XY}. Both plots are presented in dimensionless units.

last term in (23)), while the contribution given by $\frac{1}{|\omega|}\int_\omega \rho(u_x \frac{\partial u_x}{\partial x} + u_y \frac{\partial u_x}{\partial y}) y \, d\omega$ (XY component of the first term in (23)), is two orders of magnitude smaller.

4.3. Validation against direct numerical simulation

The third case studied was a fully-developed flow in a rectangular channel partially filled with obstacles. This case was used to compare the solution delivered by the multi-scale model with the solution produced by DNS. In this case, the comparison is facilitated because the analytical solution for the coarse-scale flow model can be computed, provided we assume linearity in the relation between C_X, Σ_{XY} and U_X, G_{XY}. Such hypothesis is valid in view of the findings reported in Section 4.2 (see Fig. 8).

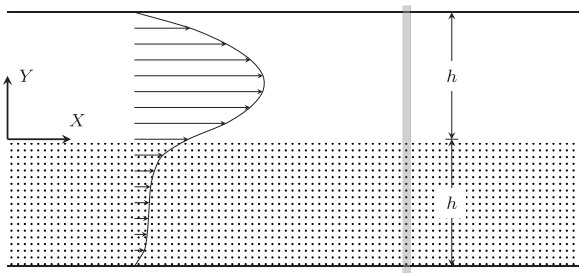

Fig. 9. Illustrative scheme of the problem of flow between parallel plates with half of the cross section filled with circular obstacles. The gray area highlights the domain of analysis (see details in Fig. 10).

Consider the flow of a fluid between two parallel plates where part of the cross section is obstructed by a permeable medium consisting of an array circular obstacles, as shown in Fig. 9.

The origin of the transversal coordinate, $Y = 0$, is located at the center of the channel cross section, coinciding with the edge of the permeable medium. Assuming steady-state flow fully developed in the axial direction X, the coarse-scale flow equation reduces to

$$\frac{d\Sigma_{XY}}{dY} - C_X = \frac{dP}{dX}. \tag{41}$$

The homogenized magnitudes Σ_{XY} and C_X depend in general on U_X and $G_{XY} = \frac{dU_X}{dY}$, where U_X is the axial component of the fully-developed coarse scale velocity field ($U_Y = 0$). As seen in the previous section, due to the symmetry of the RVE, inside the permeable region ($y < 0$) these dependences boil down to

$$\Sigma_{XY} = \mu_e \frac{dU_X}{dY}, \tag{42}$$

$$C_X = \frac{\mu}{\kappa} U_X, \tag{43}$$

whereas in the free-flow region ($y > 0$) it is

$$\Sigma_{XY} = \mu \frac{dU_X}{dY}, \tag{44}$$

$$C_X = 0. \tag{45}$$

Combining Eqs. (41)–(45) leads to the following ordinary differential equation for $U_X(Y)$

$$\tilde{\mu}_e \frac{d^2U_X}{dY^2} - \frac{H(Y)}{\kappa} U_X = \frac{1}{\mu}\frac{dP}{dX}, \tag{46}$$

where

$$H(Y) = \begin{cases} 0 & 0 < y < h, \\ 1 & -h < y < 0. \end{cases} \tag{47}$$

Eq. (46) has the following analytic solution (see for example [39])

$$U_X(Y) = \begin{cases} -\dfrac{U_o}{2}\left(\dfrac{Y}{h}\right)^2 + A\dfrac{Y}{h} + B & 0 < y < h, \\ U_o\dfrac{\kappa}{h^2} + C\cosh\left(\dfrac{Y}{Y_o}\right) + D\sinh\left(\dfrac{Y}{Y_o}\right) & -h < y < 0, \end{cases} \tag{48}$$

where

$$U_o = -\frac{h^2}{\mu}\frac{dP}{dX}, \tag{49}$$

$$Y_o = \sqrt{\kappa\tilde{\mu}_e}, \tag{50}$$

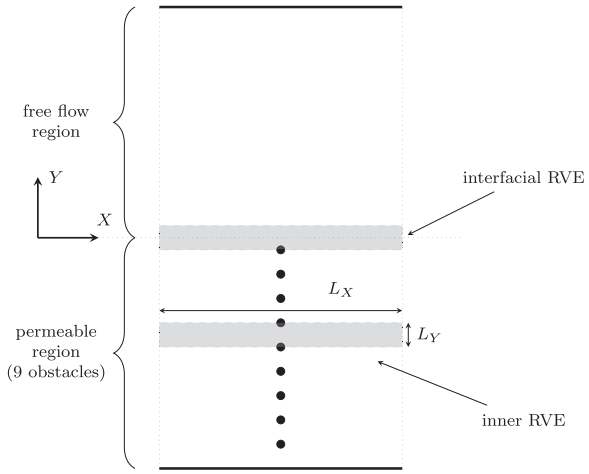

Fig. 10. Details of the array of obstacles in the channel (gray area highlighted in Fig. 9). The shaded regions depict the RVE at the interface between free flow and permeable media, and an inner RVE within the permeable medium.

and A, B, C, D to be determined through proper boundary and coupling conditions. Over the plates ($Y = \pm h$), the no-slip condition implies

$$U_X(-h) = U_X(h) = 0. \tag{51}$$

In turn, the coupling conditions at the interface ($Y = 0$) is a long-time problem that has for many years received, and still receives, considerable attention [40–50]. Within the present modeling approach, it will be assumed continuity of velocity and of stress, that is

$$U_X(0^-) = U_X(0^+), \tag{52}$$

$$\Sigma_{XY}(0^-) = \Sigma_{XY}(0^+). \tag{53}$$

It should be noted that the stress should be modeled for the RVE of the interface (see Fig. 10). Such RVE is not symmetric because there is no obstacle on the side facing the free flow, which induces an imbalance of the moment of the drag forces with respect to the centerline of the RVE, causing the appearance of a stress term proportional to the velocity. That is, instead of (42) the following relation between Σ_{XY} and (U_X, G_{XY}) is rendered by the homogenization procedure

$$\Sigma_{XY}(0^-) = \mu_b \frac{dU_X}{dY}(0^-) + \frac{\mu}{\ell_b} U_X(0^-), \tag{54}$$

where μ_b is the effective viscosity of the interfacial RVE and ℓ_b is a length parameter accounting for the asymmetry of the drag. Combining Eqs. (44), (53) and (54) leads to the following coupling condition at the interface

$$\mu_b \frac{dU_X}{dY}(0^-) + \frac{\mu}{\ell_b} U_X(0^-) = \mu U_X(0^+). \tag{55}$$

Using (51), (52) and (55), the coefficients in (48) result

$$A = \frac{U_o}{2} - U_i, \quad B = U_i, \quad C = U_i - \frac{\kappa}{h^2} U_o, \quad D = \frac{\mu Y_o}{\mu_b h}\left[\frac{U_o}{2} - U_i\left(1 + \frac{h}{\ell_b}\right)\right], \tag{56}$$

where

$$U_i = U_o \left[\frac{\frac{1}{2}\sinh\left(\frac{h}{Y_o}\right) + \frac{Y_o}{h}\left(\cosh\left(\frac{h}{Y_o}\right) - 1\right)}{\left(1 + \frac{h}{\ell_b}\right)\sinh\left(\frac{h}{Y_o}\right) + \frac{\mu_b h}{\mu Y_o}\cosh\left(\frac{h}{Y_o}\right)}\right], \tag{57}$$

is the velocity at $Y = 0$.

Table 1
Homogenized parameters obtained from the fine scale problem (RVE problem) for the semi-permeable channel shown in Fig. 10. The parameter d is the diameter of the obstacles, L_X and L_Y are the sizes of the sides of the RVE, κ is the permeability, μ_e is the effective viscosity, and ℓ_b is the length parameter appearing in Eq. (55).

d/L_Y	$\kappa/(L_X L_Y)$	μ_e/μ	μ_b/μ	ℓ_b/L_Y
1/4	0.040	1.33	1.20	−0.40
1/5	0.058	1.27	1.17	−0.34

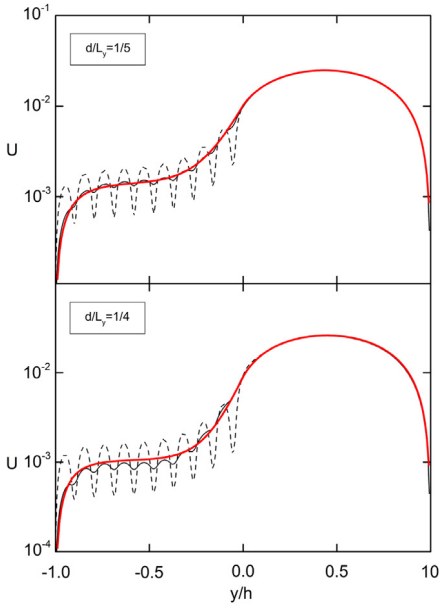

Fig. 11. Fully-developed flow velocity profile (log scale) across the channel for arrays with 9 obstacles of two different sizes d. The black curves are the DNS solutions, averaged along the X coordinate over the whole X run of the RVE (solid curve) and averaged only over a length L_Y around the obstacles (dashed curve). The red lines are the coarse scale (analytical) solutions produced with the parameters delivered by the fine scale problem, which are reported in Table 1.

Table 1 lists the values of the parameters of the interfacial RVE for two different obstacle sizes characterized by the obstacle diameter d.

The red curves in Fig. 11 are the solutions of the coarse scale flow model. These solutions are produced by the parameters of Table 1 that define the relation between (C_X, Σ_{XY}) and (U_X, G_{XY}) which are rendered by the fine scale problem. In order to assess the degree of approximation of the proposed multi-scale model, the complete velocity field at the fine scale was calculated by DNS. Fig. 11 also shows the DNS solution averaged along the X coordinate over the whole run of the RVE (solid curve with small oscillations) and averaged only over a length L_Y at the center around the obstacles (dashed curve with large oscillations). Clearly, the multi-scale model is able to retrieve most of the coarse scale physics in the homogenized sense. The most challenging aspect in this regard is the transition between the free flow region and the permeable media, which is well predicted by the multi-scale model.

5. Concluding remarks

In this work we have proposed a multi-scale model to simulate complex phenomena in fluid flow problems using the concept of representative volume element. The foundations for the methodology are established by the Method of Multi-scale Virtual Power, which allows a consistent and natural derivation of homogenization formulae of coarse scale force- and stress-like entities from purely kinematic assumptions (conservation of velocity and conservation of velocity gradient). The model was tested in steady state problems characterized by different flow conditions, featuring excellent predictive capabilities in controlled scenarios as well as in comparisons against direct numerical simulations.

Remarkably, the model behaved accurately in the homogenized sense even in challenging cases such as those posed by a fluid flowing amid obstacles in permeable media close to interfaces with free flows. Finally, the proposed approach can be extended to deal with time-dependent phenomena as well as with moving objects. These cases are being matter of current research.

Acknowledgments

This work was partially supported by the Brazilian agencies CNPq and FAPERJ. The support of these agencies is gratefully acknowledged.

Appendix. Explicit characterization of homogenized entities

Let us show in this section that the characterizations of $\mathbf{C}$ and $\boldsymbol{\Sigma}$ given by (21) and (23), respectively, hold.

Consider for simplicity that $\int_\omega \mathbf{x}\, d\omega = \mathbf{0}$. In the RVE domain, and without loss of generality, the velocity field $\mathbf{u}$ can be expanded as follows

$$\mathbf{u} = \mathbf{U} + \mathbf{G}\mathbf{x} + \tilde{\mathbf{u}}, \tag{58}$$

where, $\mathbf{U}$ and $\mathbf{G}$ are information from the coarse scale, and $\tilde{\mathbf{u}}$ is a fluctuation field. Then, we have

$$\nabla_\omega \mathbf{u} = \mathbf{G} + \nabla_\omega \tilde{\mathbf{u}}, \tag{59}$$

where ∇_ω is the gradient operator with respect to coordinates $\mathbf{x} \in \omega$.

By using (58), we have that (7) is satisfied provided that

$$\int_\omega \tilde{\mathbf{u}}\, d\omega = \mathbf{0}. \tag{60}$$

Analogously, using (58), (8) is satisfied if

$$\int_\omega \nabla_\omega \tilde{\mathbf{u}}\, d\omega = \mathbf{0}, \tag{61}$$

or equivalently, integrating by parts,

$$\int_{\partial\omega} \tilde{\mathbf{u}} \otimes \mathbf{n}\, d\partial\omega = \mathbf{0}. \tag{62}$$

Also, the velocity field $\mathbf{u}$ is divergence-free, i.e. satisfies (5), and has to satisfy the no-slip condition over obstacles (6), therefore, the fluctuation field satisfies the following two constraints

$$\mathrm{div}_\omega \tilde{\mathbf{u}} = 0 \quad \text{in } \omega, \tag{63}$$

$$\tilde{\mathbf{u}} = -(\mathbf{U} + \mathbf{G}\mathbf{x}) \quad \text{on } \gamma. \tag{64}$$

Thus, we define the linear manifold of kinematically admissible velocity fluctuation fields at fine scale

$$\tilde{\mathcal{U}}_\omega = \left\{ \tilde{\mathbf{u}} \in [H^1(\omega)]^n,\ \tilde{\mathbf{u}} = -(\mathbf{U} + \mathbf{G}\mathbf{x}) \text{ on } \gamma,\ \mathrm{div}_\omega\, \tilde{\mathbf{u}} = 0 \int_\omega \tilde{\mathbf{u}}\, d\omega = \mathbf{0},\ \int_{\partial\omega} \tilde{\mathbf{u}} \otimes \mathbf{n}\, d\partial\omega = \mathbf{0} \right\}, \tag{65}$$

and, then, we have the associated linear space of kinematically admissible variations of the fluctuations field

$$\tilde{\mathcal{V}}_\omega = \left\{ \hat{\tilde{\mathbf{u}}} \in [H^1(\omega)]^n,\ \hat{\tilde{\mathbf{u}}} = -(\hat{\mathbf{U}} + \hat{\mathbf{G}}\mathbf{x}) \text{ on } \gamma,\ \mathrm{div}_\omega\, \hat{\tilde{\mathbf{u}}} = 0 \int_\omega \hat{\tilde{\mathbf{u}}}\, d\omega = \mathbf{0},\ \int_{\partial\omega} \hat{\tilde{\mathbf{u}}} \otimes \mathbf{n}\, d\partial\omega = \mathbf{0} \right\}. \tag{66}$$

These sets impose minimal kinematic restrictions to fluctuation fields such that transition between scales is consistent. Furthermore, proper functional spaces $\tilde{\mathcal{V}}^*_\omega \subset \tilde{\mathcal{V}}_\omega$ are allowed. For example, periodic boundary conditions for the fluctuation fields are the most popular choice in the multi-scale literature.

Now, the Principle of Multiscale Virtual Power formulated in (16) is written using decomposition (58). Then, the problem amounts to find $\tilde{\mathbf{u}} \in \tilde{\mathcal{U}}_\omega$ such that

$$\mathbf{C}\cdot\hat{\mathbf{U}} + \boldsymbol{\Sigma}\cdot\hat{\mathbf{G}} = \frac{1}{|\omega|}\int_\omega \left[\rho(\nabla_\omega\mathbf{u})\mathbf{u}\cdot\left(\hat{\mathbf{U}}+\hat{\mathbf{G}}\mathbf{x}+\hat{\tilde{\mathbf{u}}}\right) + 2\mu\nabla^S_\omega\mathbf{u}\cdot\left(\hat{\mathbf{G}}+\nabla_\omega\hat{\tilde{\mathbf{u}}}\right)\right]d\omega$$
$$\forall(\hat{\mathbf{U}},\hat{\mathbf{G}},\hat{\tilde{\mathbf{u}}}) \in \mathbb{R}^n\times\mathbb{T}^{n\times n}\times\tilde{\mathcal{V}}_\omega. \tag{67}$$

Now, the no-slip constraint and the divergence constraint are relaxed using proper Lagrange multipliers $\mathbf{r}$ and p, respectively. This yields the following problem find $\tilde{\mathbf{u}} \in \tilde{\mathcal{U}}^\circ_\omega$ such that

$$\mathbf{C}\cdot\hat{\mathbf{U}} + \boldsymbol{\Sigma}\cdot\hat{\mathbf{G}} = \frac{1}{|\omega|}\left[\int_\omega \left[\rho(\nabla_\omega\mathbf{u})\mathbf{u}\cdot\left(\hat{\mathbf{U}}+\hat{\mathbf{G}}\mathbf{x}+\hat{\tilde{\mathbf{u}}}\right) + 2\mu\nabla^S_\omega\mathbf{u}\cdot\left(\hat{\mathbf{G}}+\nabla_\omega\hat{\tilde{\mathbf{u}}}\right)\right]d\omega\right.$$
$$\left. + \int_\gamma \mathbf{r}\cdot\left(\hat{\mathbf{U}}+\hat{\mathbf{G}}\mathbf{x}+\hat{\tilde{\mathbf{u}}}\right)d\gamma + \int_\gamma \hat{\mathbf{r}}\cdot\mathbf{u}\,d\gamma - \int_\omega p\,\mathrm{div}_\omega\,\hat{\tilde{\mathbf{u}}}\,d\omega - \int_\omega \hat{p}\,\mathrm{div}_\omega\,\tilde{\mathbf{u}}\,d\omega\right]$$
$$\forall(\hat{\mathbf{U}},\hat{\mathbf{G}},\hat{\tilde{\mathbf{u}}}) \in \mathbb{R}^n\times\mathbb{T}^{n\times n}\times\tilde{\mathcal{U}}^\circ_\omega\ \forall(\hat{p},\hat{\mathbf{r}}) \in \times L^2(\omega)\times[H^{-1/2}(\gamma)]^n, \tag{68}$$

where

$$\tilde{\mathcal{U}}^\circ_\omega = \left\{\tilde{\mathbf{u}}\in[H^1(\omega)]^n,\ \int_\omega\tilde{\mathbf{u}}\,d\omega = \mathbf{0},\ \int_{\partial\omega}\tilde{\mathbf{u}}\otimes\mathbf{n}\,d\partial\omega = \mathbf{0}\right\}. \tag{69}$$

The Euler–Lagrange equations associated to (68) are the following.

- Consider in (68) that $\hat{\mathbf{U}} = \mathbf{0}$ and $\hat{\mathbf{G}} = \mathbf{0}$, then

$$\int_\omega\left[\rho(\nabla_\omega\mathbf{u})\mathbf{u}\cdot\hat{\tilde{\mathbf{u}}} + 2\mu\nabla^S_\omega\mathbf{u}\cdot\nabla_\omega\hat{\tilde{\mathbf{u}}} - p\,\mathrm{div}_\omega\,\hat{\tilde{\mathbf{u}}} - \hat{p}\,\mathrm{div}_\omega\,\tilde{\mathbf{u}}\right]d\omega + \int_\gamma\mathbf{r}\cdot\hat{\tilde{\mathbf{u}}}\,d\gamma + \int_\gamma\hat{\mathbf{r}}\cdot\mathbf{u}\,d\gamma = 0$$
$$\forall(\hat{\tilde{\mathbf{u}}},\hat{p},\hat{\mathbf{r}}) \in \tilde{\mathcal{U}}^\circ_\omega\times\times L^2(\omega)\times[H^{-1/2}(\gamma)]^n. \tag{70}$$

- Consider now that in (68) it is just $\hat{\mathbf{U}} \neq \mathbf{0}$, then

$$\mathbf{C}\cdot\hat{\mathbf{U}} = \frac{1}{|\omega|}\left[\int_\omega\rho(\nabla_\omega\mathbf{u})\mathbf{u}\cdot\hat{\mathbf{U}}\,d\omega + \int_\gamma\mathbf{r}\cdot\hat{\mathbf{U}}\,d\gamma\right]\quad\forall\hat{\mathbf{U}}\in\mathbb{R}^n, \tag{71}$$

and therefore

$$\mathbf{C} = \frac{1}{|\omega|}\left[\int_\omega\rho(\nabla_\omega\mathbf{u})\mathbf{u}\,d\omega + \int_\gamma\mathbf{r}\,d\gamma\right]. \tag{72}$$

- Finally, consider in (68) that just $\hat{\mathbf{G}} \neq \mathbf{0}$, then

$$\boldsymbol{\Sigma}\cdot\hat{\mathbf{G}} = \frac{1}{|\omega|}\left[\int_\omega\left[\rho(\nabla_\omega\mathbf{u})\mathbf{u}\cdot\left(\hat{\mathbf{G}}\mathbf{x}\right) + 2\mu\nabla^S_\omega\mathbf{u}\cdot\hat{\mathbf{G}}\right]d\omega + \int_\gamma\mathbf{r}\cdot\left(\hat{\mathbf{G}}\mathbf{x}\right)d\gamma\right]\quad\forall\hat{\mathbf{G}}\in\mathbb{T}^{n\times n} \tag{73}$$

and, noting that for any vectors $\mathbf{a}$, $\mathbf{b}$ and for any second order tensor $\mathbf{A}$ it is $\mathbf{a}\cdot\mathbf{A}\mathbf{b} = (\mathbf{a}\otimes\mathbf{b})\cdot\mathbf{A}$, we have

$$\boldsymbol{\Sigma} = \frac{1}{|\omega|}\left[\int_\omega\left[\rho(\nabla_\omega\mathbf{u})\mathbf{u}\otimes\mathbf{x} + 2\mu\nabla^S_\omega\mathbf{u}\right]d\omega + \int_\gamma\mathbf{r}\otimes\mathbf{x}\,d\gamma\right]^D, \tag{74}$$

where $(\cdot)^D$ denotes the deviatoric component of tensor $(\cdot)$.

The characterization of $\mathbf{C}$ and $\boldsymbol{\Sigma}$ given by (72) and (74) is general regardless the choice of the kinematical constraints adopted for the fluctuation field in (69).

References

[1] E. Bafekrpour, A. Dyskin, E. Pasternak, A. Molotnikov, Y. Estrin, Internally architectured materials with directionally asymmetric friction, Sci. Rep. 5 (2015) 10732.
[2] J. Christensen, F. García de Abajo, Anisotropic metamaterials for full control of acoustic waves, Phys. Rev. Lett. 108 (2012) 124301.

[3] M. Maldovan, Sound and heat revolutions in phononics, Nature 503 (2013) 209–217.
[4] J. Zhu, J. Christensen, J. Jung, L. Martin-Moreno, X. Yin, L. Fok, X. Zhang, F. Garcia-Vidal, A holey-structured metamaterial for acoustic deep-subwavelength imaging, Nat. Phys. 7 (2011) 52–55.
[5] C. Zhu, T. Han, E. Duoss, A. Golobic, J. Kuntz, C. Spadaccini, M. Worsley, Highly compressible 3D periodic graphene aerogel microlattices, Nature Commun. 6 (2015) 6962.
[6] G. Buckinx, M. Baelmans, Multi-scale modelling of flow in periodic solid structures through spatial averaging, J. Comput. Phys. 291 (2015) 34–51.
[7] M. Griebel, M. Klitz, Homogenization and numerical simulation of flow in geometries with textile microstructures, Multiscale Model. Simul. 8 (2010) 1439–1460.
[8] M. Icardi, G. Boccardo, D. Marchisio, T. Tosco, R. Sethi, Pore-scale simulation of fluid flow and solute dispersion in three-dimensional porous media, Phys. Rev. E 90 (2014) 013032.
[9] M. Quintard, S. Whitaker, Transport in ordered and disordered porous media II: generalized volume averaging, Transp. Porous Media 14 (1994) 179–206.
[10] Z. Yao, H. Zhao, Homogenization of a stationary Navier-Stokes flow in porous medium with thin film, Acta Math. Sci. 28 (2008) 963–974.
[11] G. Allaire, Homogenization of the Navie–Stokes equations in open sets perforated with tiny holes. I. Abstract framework, a volume distribution of holes, Arch. Ration. Mech. Anal. 113 (1991) 209–259.
[12] G. Allaire, Homogenization of the Navier-Stokes equations in open sets perforated with tiny holes. II. Noncritical sizes of the holes for a volume distribution and a surface distribution of holes, Arch. Ration. Mech. Anal. 113 (1991) 261–298.
[13] G. Allaire, Homogenization and two-scale convergence, SIAM J. Math. Anal. 23 (1992) 1482–1518.
[14] D. Brown, P. Popov, Y. Efendiev, On homogenization of stokes flow in slowly varying media with applications to fluid–structure interaction, Int. J. Geomath. 2 (2011) 281–305.
[15] E. Feireisl, Y. Namlyeyeva, S. Necasová, Homogenization of the evolutionary Navier-Stokes system, Manuscripta Math 149 (2015) 251–274.
[16] E. Feireisl, A. Novotný, T. Takahashi, Homogenization and singular limits for the complete Navier-Stokes-Fourier system, J. Math. Pures Appl. 94 (2010) 33–57.
[17] A. Mikelić, Homogenization of nonstationary Navier-Stokes equations in a domain with a grained boundary, Ann. Mat. Pura Appl. 158 (1991) 167–179.
[18] G. Nguetseng, L. Signing, Sigma-convergence of stationary Navier-Stokes type equations, Electron. J. Differential Equations 74 (2009) 1–18.
[19] H. Zhao, Homogenization of the incompressible Navier-Stokes fluid with oscillation coefficient, Acta Math. Sci. 34 (2014) 183–193.
[20] T. Hou, X. Hu, Multiscale modeling of incompressible turbulent flows, J. Comput. Phys. 232 (2013) 383–396.
[21] R. Hill, On constitutive macro-variables for heterogeneous solids at finite strain, Proc. R. Soc. Lond. Ser. A Math. Phys. Eng. Sci. 326 (1972) 131–147.
[22] J. Mandel, Plasticité Classique et Viscoplasticité, in: CISM Lecture Notes, vol. 97, Springer-Verlag, Udine, Italy, 1971.
[23] F. Feyel, J. Chaboche, Fe2 multiscale approach for modelling the elastoviscoplastic behaviour of long fibre SiC/Ti composite materials, Comput. Methods Appl. Mech. Engrg. 183 (2000) 309–330.
[24] P. Kanouté, D.P. Boso, J. Chaboche, B. Schrefler, Multiscale methods for composites: a review, Arch. Comput. Methods Eng. 16 (2009) 31–75.
[25] V. Kouznetsova, W. Brekelmans, F. Baaijens, An approach to micro-macro modeling of heterogeneous materials, Comput. Mech. 27 (2001) 37–48.
[26] C. Miehe, J. Schotte, J. Schröder, Computational micro-macro transitions and overall moduli in the analysis of polycrystals at large strains, Comput. Mater. Sci. 6 (1999) 372–382.
[27] S. Nemat-Nasser, Averaging theorems in finite deformation plasticity, Mech. Mater. 31 (1999) 493–523.
[28] C. Sandstrom, F. Larsson, Variationally consistent homogenization of Stokes flow in porous media, Int. J. Multiscale Com. 11 (2013) 117–138.
[29] P.J. Blanco, P.J. Sánchez, E.A. de Souza Neto, R.A. Feijóo, Variational foundations and generalized unified theory of RVE-based multiscale models, Arch. Comput. Methods Eng. 23 (2016) 191–253.
[30] E.A. de Souza Neto, P.J. Blanco, P.J. Sánchez, R.A. Feijóo, An RVE-based multiscale theory of solids with micro-scale inertia and body force effects, Mech. Mater. 80 (2015) 136–144.
[31] P.J. Blanco, P.J. Sánchez, E.A. de Souza Neto, R.A. Feijóo, The method of multiscale virtual power for the derivation of a second order mechanical model, Mech. Mater. 99 (2016) 53–67.
[32] P.J. Blanco, S.M. Giusti, Thermomechanical multiscale constitutive modeling: accounting for microstructural thermal effects, J. Elasticity 115 (2014) 27–46.
[33] P.J. Sánchez, P.J. Blanco, A.E. Huespe, R.A. Feijóo, Failure-Oriented Multi-scale Variational Formulation: Micro-structures with nucleation and evolution of softening bands, Comput. Methods Appl. Mech. Engrg. 257 (2013) 221–247.
[34] S. Toro, P.J. Sánchez, P.J. Blanco, E.A. de Souza Neto, A.E. Huespe, R.A. Feijóo, Multiscale formulation for material failure accounting for cohesive cracks at the macro and micro scales, Int. J. Plast. 76 (2016) 75–110.
[35] G. Boroni, N. Silin, D. Dalponte, J. Dottori, A. Clausse, Lattice-Boltzmann modeling of unstable flows amid arrays of wires, Comput. Fluids 37–45 (2015) 120.
[36] X. He, L. Luo, Theory of the lattice Boltzmann method: From the Boltzmann equation to the lattice Boltzmann equation, Phys. Rev. E 56 (1997) 6811–6817.
[37] A. Mohamad, A. Kuzmin, A critical evaluation of force term in lattice Boltzmann method, natural convection problem, Int. J. Heat Mass Transfer 53 (2010) 990–996.
[38] R.C. Givler, S.A. Altobelli, A determination of the effective viscosity for the Brinkman-Forchheimer flow model, J. Fluid Mech. 258 (1994) 355–370.
[39] Y. Gayev, Easily penetrable roughnesses of different structures, in: Y. Gayev, J. Hunt (Eds.), Flow and Transport Processes With Complex Obstructions, Springer, The Netherlands, 2007, pp. 89–178. (Chapter 3).

[40] B. Alazmi, K. Vafai, Analysis of fluid flow and heat transfer interfacial conditions between a porous medium and a fluid layer, Int. J. Heat Mass Transfer 44 (2001) 1735–1749.
[41] M. Chandesris, D. Jamet, Boundary conditions at a planar fluid-porous interface for a Poiseuille flow, Int. J. Heat Mass Transfer 49 (2006) 2137–2150.
[42] M. Chandesris, D. Jamet, Boundary conditions at a fluid-porous interface: An a priori estimation of the stress jump coefficients, Int. J. Heat Mass Transfer 50 (2007) 3422–3436.
[43] A. Goharzadeh, A. Khalili, B. Jørgensen, Transition layer thickness at a fluid-porous interface, Phys. Fluids 17 (2005) 057102.
[44] B. Goyeau, D. Lhuillier, D. Gobin, M. Velarde, Momentum transport at a fluid-porous interface, Int. J. Heat Mass Transfer 46 (2003) 4071–4081.
[45] J. Ochoa-Tapia, Momentum transfer at the boundary between a porous medium and a homogeneous fluid I. Theoretical development, Int. J. Heat Mass Transfer 38 (1995) 2635–2646.
[46] J. Ochoa-Tapia, Momentum transfer at the boundary between a porous medium and a homogeneous fluid II. Comparison with experiment, Int. J. Heat Mass Transfer 38 (1995) 2647–2655.
[47] M. Sahraoui, M. Kaviany, Slip and no-slip velocity boundary conditions at the interface of porous plain media, Int. J. Heat Mass Transfer 35 (1992) 927–943.
[48] K. Vafai, S. Kim, On the limitations of the Brinkman-Forchheimer-extended Darcy equation, Internat. J. Heat Fluid Flow 16 (1995) 11–15.
[49] F. Valdés-Parada, B. Goyeau, J. Ochoa-Tapia, Jump momentum boundary condition at a fluid-porous dividing surface: Derivation of the closure problem, Chem. Eng. Sci. 62 (2007) 4025–4039.
[50] F. Valdés-Parada, J. Ochoa-Tapia, J. Alvarez-Ramirez, On the effective viscosity for the Darcy–Brinkman equation, Phys. A 385 (2007) 69–79.